MDPI

Article

Porous Ni Photocathodes Obtained by Selective Corrosion of Ni-Cu Films: Synthesis and Photoelectrochemical Characterization

Laura Mais [1], Simonetta Palmas [1], Michele Mascia [1], Elisa Sechi [1], Maria Francesca Casula [1], Jesus Rodriguez [2] and Annalisa Vacca [1,*]

[1] Chimica e dei Materiali, Dipartimento di Ingegneria Meccanica, Università degli studi di Cagliari, via Marengo 2, 09123 Cagliari, Italy; l.mais@dimcm.unica.it (L.M.); simonetta.palmas@dimcm.unica.it (S.P.); michele.mascia@unica.it (M.M.); elisa.sechi85@gmail.com (E.S.); casulaf@unica.it (M.F.C.)

[2] Centro Nacional del Hidrógeno (CNH2). Prolongación Fernando El Santo s/n, Puertollano, 13500 Ciudad Real, Spain; jesus.rodriguez@cnh2.es

[*] Correspondence: annalisa.vacca@dimcm.unica.it; Tel.: +39-070-6755-059

check for updates

Abstract: In this work, a dealloying technique is proposed as a synthesis method to obtain highly porous Nickel electrodes starting from Ni-Cu co-deposit: pulsed corrosion is applied adopting different corrosion and relaxation times. Different morphologies, pore size distribution and residual copper amount were obtained depending on the corrosion conditions. For the developed electrodes, the surface roughness factor, R_f, was evaluated by electrochemical impedance spectroscopy (EIS). The hydrogen evolution reaction (HER) on these electrodes was evaluated by means of steady-state polarization curves, and the related parameters were derived by Tafel analysis. Finally, a thin layer of NiO on the porous structures was obtained to exploit the semiconductor characteristic of the oxide, so that an extra-photopotential was obtained by the simulated solar light action. Results demonstrate greater apparent activity of the developed electrodes towards HER in comparison with commercial smooth Ni electrode, which can be mainly attributed to the large R_f obtained with the proposed technique.

Keywords: porous nickel; selective corrosion; hydrogen evolution reaction; photoelectrocatalysis

1. Introduction

The production of hydrogen by electrocatalytic or photoelectrocatalytic (PEC) water splitting driven by renewable energy, and its subsequent use in a fuel cell, could represent a zero-emission process in which the storage of H_2 could mitigate the spatial and temporal discontinuities of renewable energy resources [1,2]. However, due to the high overpotential losses involved in the gas evolution reactions occurring at the electrodes, the electrolytic H_2 production is still not competitive, at large scale, with the traditional process of H_2 production from fossil fuels [3]. In fact, noble metals such as Pt, Ru, and Pd are ideal electrocatalysts for hydrogen evolution reaction (HER) in terms of overpotential. Nevertheless, high cost and scarcity make them impractical choices, and the quest for finding inexpensive electrocatalysts is indeed an active area of research [3].

Although many earth-abundant HER catalysts such as transition metal chalcogenides [4,5] or carbides [6,7] have exhibited high activities in acid solutions approaching that of Pt, all of them cannot operate satisfactorily in alkaline electrolytes [8]. Recently, nickel-based electrocatalysts, either as monofunctional or bifunctional materials, were proposed as an economical and efficient replacement to these expensive metal precursors, that exhibited very promising electrocatalytic activity and stability toward oxygen and hydrogen evolution reactions [9–12].

Due to its electronic properties, high conductivity, and thermal stability, Ni has been a very frequent choice for designing electrocatalytic materials. Ni and its related oxides and hydroxides have also been proposed as cathode materials which are effective for HER in non-acidic solutions [13]. Moreover, the NiO p-type semiconductor has emerged as the most frequently used material in this field for its low cost, good stability, and suitable band position alignment, for the transfer of photogenerated holes to counter electrode, that is a key efficiency-determining step of PEC water splitting [14–16]. In order to increase the catalytic activity of nickel based materials towards the HER, two basic approaches could be adopted, namely the use of multicomponent catalysts and the increase of the real surface area [17]. Ni-based alloys, together with other transition metals or rare earths, have been widely studied and exhibited better catalytic capability than single Ni catalyst, due to synergistic effects of the elements forming the alloy [18,19]. Among the Ni-based alloy electrodes studied, Ni–Cu alloy has shown potential as cathode for alkaline HER due to the improved electrocatalytic activity [20,21], high corrosion resistance [22] and good stability [23].

As already stated, the second way to increase the catalytic activity is the preparation of an electrode with a high surface area, that represents a crucial point to which attention should be paid to achieve high efficiency [24–26]. However, the synthesis of ordered nanoporous metals faces great challenges, since metals at the nanoscale tend to present low surface area in order to minimize the surface energy [27]. Moreover, the simple increase of the surface area does not always reflect an increase in the electrochemically-active surface area, because the morphology and the dimension of pores may affect the accessible surface area for the electrochemical reactions.

Nickel foam with a nanoporous structure can be obtained by several methods, such as alkaline leaching of the aluminum from Ni-Al Raney nickel [28], chemical vapor deposition [29,30], electrodeposition [31] and template synthesis [32,33]. However, these processes were found to be imperfect due to limitations in controlling pore sizes and relative density which are important for metallic foams [34].

Based on the above results, in this work, the electrochemical corrosion of Cu-Ni co-deposit was selected for the fabrication of porous Ni-based electrodes, which combine both high surface area and good intrinsic catalytic activity in the process of HER. The selective electrochemical corrosion of copper from Ni_xCu_{1-x} alloy was demonstrated for the first time by Sun and co-workers; by taking advantage from the formation of a passive nickel oxide film in sulfamate aqueous solutions, nanoporous nickel was prepared through selective electrochemical dissolution of the more noble copper, rather than the less noble Ni. The authors performed electrochemical etching under potentiostatic conditions; depending on the composition of the deposited alloy, different morphologies and dimensions of the pores were obtained [35].

Similarly, Chang and co-workers obtained nano-hollow tubes starting from Ni-Cu alloys prepared by electrodeposition, which showed a columnar structure and contained separated Cu- and Ni- rich multiple phases; the selective etching of the less reactive copper from the alloys was performed in solutions containing H_3BO_3 0.5 M [36]. A dendritic Ni-Cu alloy foam with high surface area was fabricated by electrodeposition during HER by Jeong and co-workers; then nanoporous dendritic Ni foam was successfully prepared by selective electrochemical dealloying of copper from Ni-Cu alloy using a sulfuric acid solution [37]. In order to control the morphological features of the porous structure, the dealloying of a co-deposited Ni-Cu was performed under pulsed electric field. By tuning voltage and duration of the bias applied, different final composition and degree of porosity were obtained [38].

To the best of our knowledge, few works have been devoted to the systematic study of the effects of the corrosion conditions of copper on the morphology and dimensions of the pores of nickel, as well as to the amount of residual copper. In this work, we studied the effect of the dealloying conditions, with the application of a voltage waveform, on morphology, real area and composition of the resulting samples. Starting from the same deposit containing 30% of copper and 70% of nickel, different values of corrosion and relaxation times were adopted: two classes of samples were prepared with two values of the ratio between the corrosion and relaxation times.

Moreover, also the electrocatalytic performance of the developed electrodes for HER and for photoelectrochemical tests were studied. To distinguish the effect of both surface roughness and intrinsic activity of the material, the real active surface area of the catalysts, in terms of roughness factor (R_f), was determined.

2. Results and Discussion

The electrodeposition of Ni-Cu was realized under potentiostatic conditions at E = −0.8 V for 130 minutes on niobium discs; linear sweep voltammetry was firstly performed in the electrodeposition solution at 5 mV s^{-1}, starting from open circuit potential (OCP) up to −0.8 V, to favor a slow deposition of a thin film onto niobium surface.

Figure 1 displays the scanning electron microscopy (SEM) images and the Auger mappings of the Ni-Cu deposit onto the niobium surface; as can be seen, a homogeneous distribution of both the elements, with some copper agglomerations, characterized the surface. The chemical composition of the film calculated by energy dispersive X-ray (EDX) analysis indicated an average molar fraction of 30% of copper and 70% of nickel.
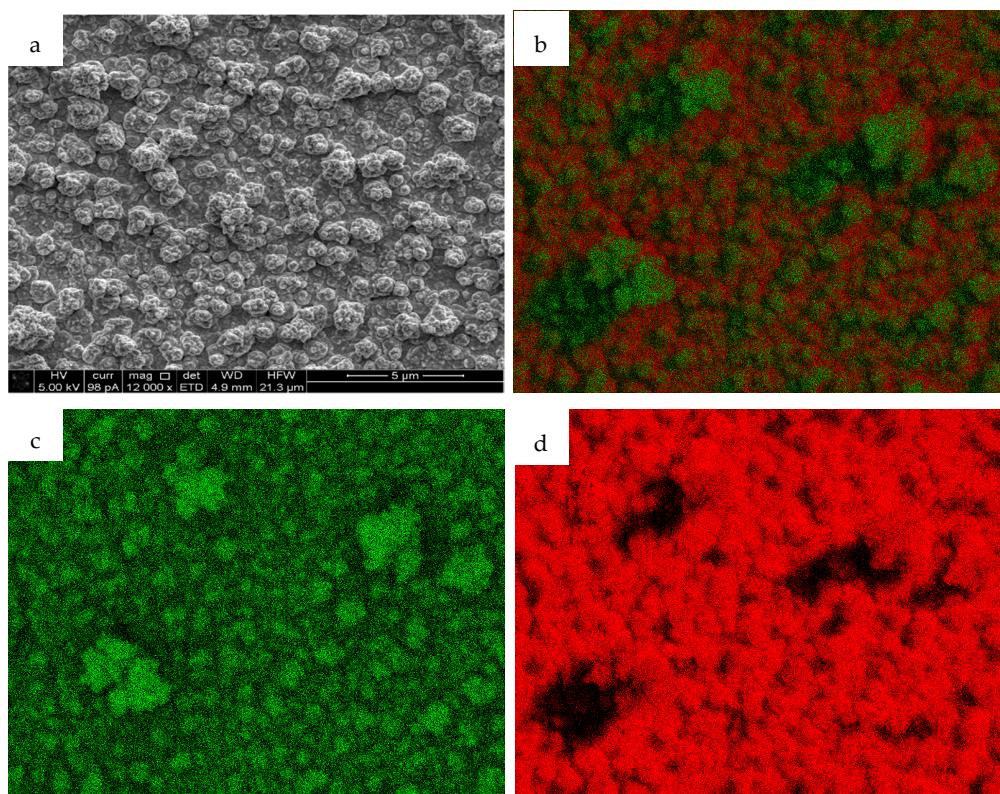

Figure 1. SEM image (**a**) and Auger mappings (**b**) of Ni-Cu deposit onto niobium substrates: Cu in green and Ni in red. The separated Auger mappings of Cu and Ni are reported in (**c**) and (**d**), respectively.

The SEM images of the samples obtained using different corrosion conditions (Figure 2), show the presence of porous structures in each sample. Table 1 reports the conditions adopted for the corrosion of each sample, denoted as $S_{tcorr\text{-}trelax}$ where t_{corr} and t_{relax} are the corrosion and relaxation times used in the pulsed corrosion steps, respectively. Table 1 also reports the ratio $\phi = t_{corr}/t_{relax}$ together with the range of pore diameters and molar fractions of Cu and Ni (oxygen was found as third element up to unit).

As can be seen from SEM images, different morphologic features can be recognized depending on the experimental conditions; samples prepared with the highest ϕ as S_{1-5} (Figure 2a) and $S_{0.1-0.5}$ (Figure 2b) were featured by a tubular structure, while the samples prepared using the lowest ϕ (S_{1-50} in Figure 2d, $S_{0.1-5}$ in Figure 2e and $S_{0.01-0.5}$ in Figure 2f) presented a cauliflower-like structure with

multi-dimensional pores. Only the sample $S_{0.01-0.05}$ (Figure 2c) is characterized by a poor pore density with very small diameters.
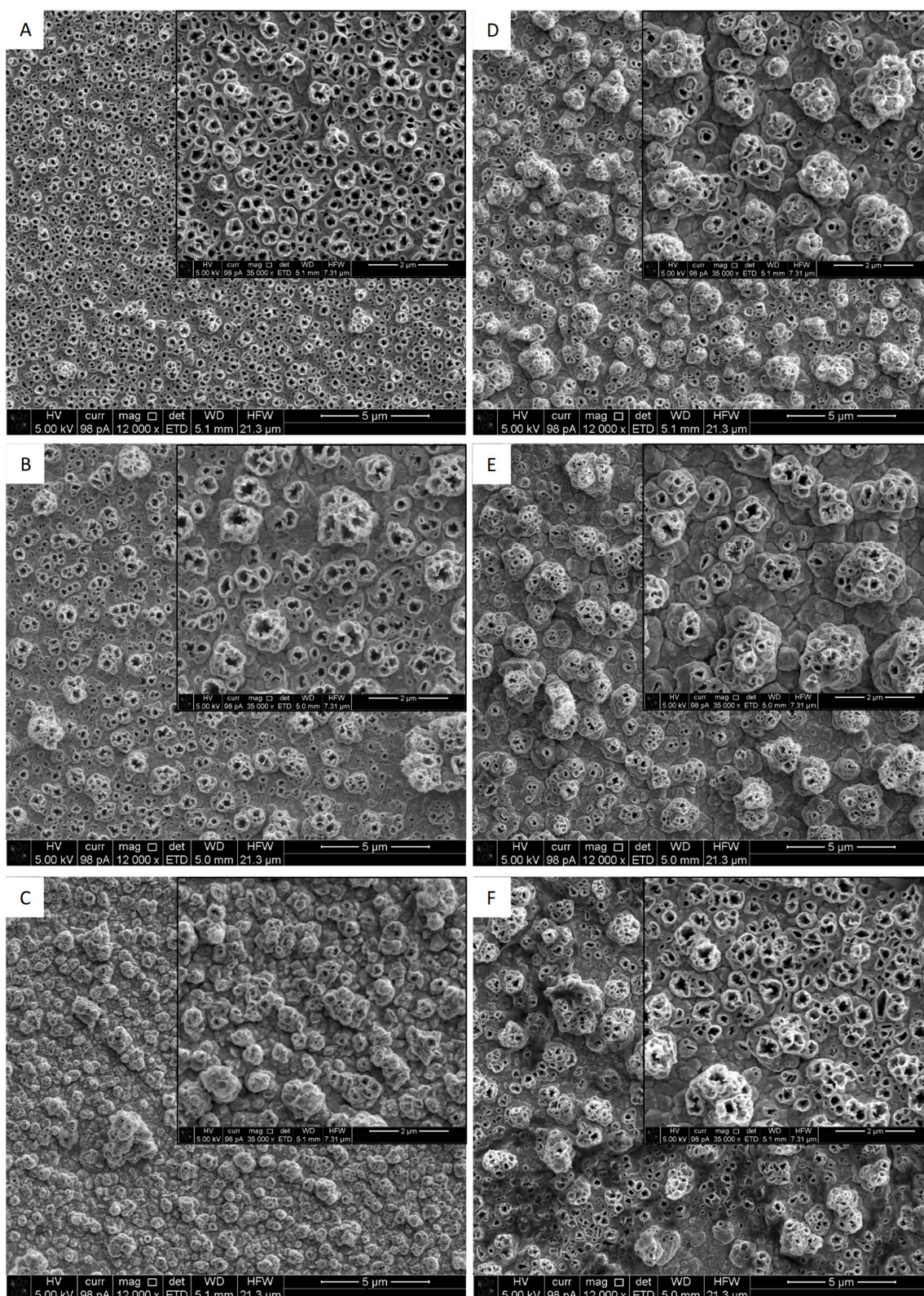
Figure 2. SEM images of samples submitted to different conditions of anodic dissolution: (**A**) S_{1-5}; (**B**) $S_{0.1-0.5}$; (**C**) $S_{0.01-0.05}$; (**D**) S_{1-50}; (**E**) $S_{0.1-5}$; (**F**) $S_{0.01-0.5}$. Insets report the magnifications of the SEM images of the samples.

Data in Table 1 and Figure 2, indicated a combined effect of t_{corr} and t_{relax} on the pore size and morphology of the resulting samples: in fact, t_{relax} being the same, a decrease in t_{corr} leads to lower pores diameter (See Figure 2 for sample S_{1-5} compared with $S_{0.1-5}$, and $S_{0.1-0.5}$ compared with $S_{0.01-0.5}$) and higher residual copper amount.

Table 1. Range of diameters d (nm) and molar fractions of Cu and Ni (X_{Cu} and X_{Ni}) of porous nickel electrodes prepared using different t_{corr} and t_{relax} during the anodic pulsed voltage dissolution experiments.

|	t_{corr}/s	t_{relax}/s	ϕ	d/nm	X_{Ni}	X_{Cu}
S_{1-5}	1	5	0.2	200–350	0.90	0.064
$S_{0.1-0.5}$	0.1	0.5	0.2	140–300	0.86	0.086
$S_{0.01-0.05}$	0.01	0.05	0.2	50–150	0.76	0.195
S_{1-50}	1	50	0.02	170–250	0.81	0.14
$S_{0.1-5}$	0.1	5	0.02	170–250	0.89	0.083
$S_{0.01-0.5}$	0.01	0.5	0.02	70–250	0.82	0.11

Conversely, an increase in t_{relax} leads to a decrease of the pores size, t_{corr} being the same, as for samples S_{1-5} and S_{1-50} (t_{corr} of 1 s), or for samples $S_{0.1-0.5}$ and $S_{0.1-5}$ (t_{corr} of 0.1 s) (See Figure 2). Moreover, in the case of t_{corr} of 0.01 s, both samples present the highest copper residual amount.

As it was firstly proposed by Erlebacher et al. [39], these results can be explained considering that the mechanism involved in the formation of porous structures, by dealloying of binary systems under potentiostatic conditions, resulted from two concurrent processes occurring at the alloy/electrolyte interface: the chemical dissolution of the most reactive metal atoms and the atom rearrangement of the most inert atoms, which expose the underlying more reactive metal atoms to further dissolution.

Using pulsed potential, it is possible to influence the interplay between atoms rearrangement and chemical dissolution [38]. Thus, the increase in the ratio ϕ favors the rearrangement of nickel with respect the copper dissolution, which in turn leads to more dendritic samples with high content of residual copper, as observed comparing samples S_{1-5} with $S_{0.1-5}$ or $S_{0.1-0.5}$ with $S_{0.01-0.5}$. Moreover, very short relaxation times, as in the case of sample $S_{0.01-0.05}$, limit the nickel atoms rearrangement thus hindering the exposure of underlying copper and its progressive dissolution: few and very small pores with very high residual copper content was obtained under this condition.

To gain insight into the structural features of the deposited films, X-ray diffraction patterns were acquired, as shown in Figure 3. The pattern of the initial deposit (Figure 3a) shows the occurrence of sharp peaks due to the niobium substrate and additional broader reflections which can be ascribed to the occurrence of nanocrystalline nickel and copper phases, based on comparison with reference PDF cards (Figure 3c). After the electrochemical corrosion, changes in the X-ray pattern can be observed in Figure 3b (sample S_{1-5}): in particular, the relative intensity of the peaks due to Ni and Cu is decreased, suggesting the occurrence of a lower contribution from nanocrystalline phases as compared to the original film. Additional peaks are also observed which can be tentatively ascribed to a copper-rich oxide (Cu_4O_3).

In order to characterise the electrodes, electrochemical impedance spectroscopy (EIS) measurements were performed in KOH 1 M solutions at open circuit potential (OCP). The related Nyquist and Bode plots are reported in Figures 4 and 5: as can be seen, samples S_{1-5}, $S_{0.01-0.05}$ and S_{1-50} are characterized by a wide flattened semicircle in the low frequency (LF) region of Nyquist plot, and by one wave in the phase angle Bode plot. This behavior is like that of smooth electrodes covered with flat pores, indicating that the surface behaves like a flat one, i.e. the pores are well accessible at all the frequency values [40,41]. For the samples $S_{0.1-0.5}$, $S_{0.1-5}$ and $S_{0.01-0.5}$ a small arc is visible at high frequency (HF), followed by a second branch in the LF region of the Nyquist plot, as well as the beginning of a second wave appears in the phase angle Bode plot, indicating a behavior typical of porous and rough electrodes [42], which respond differently, depending on the frequency region.
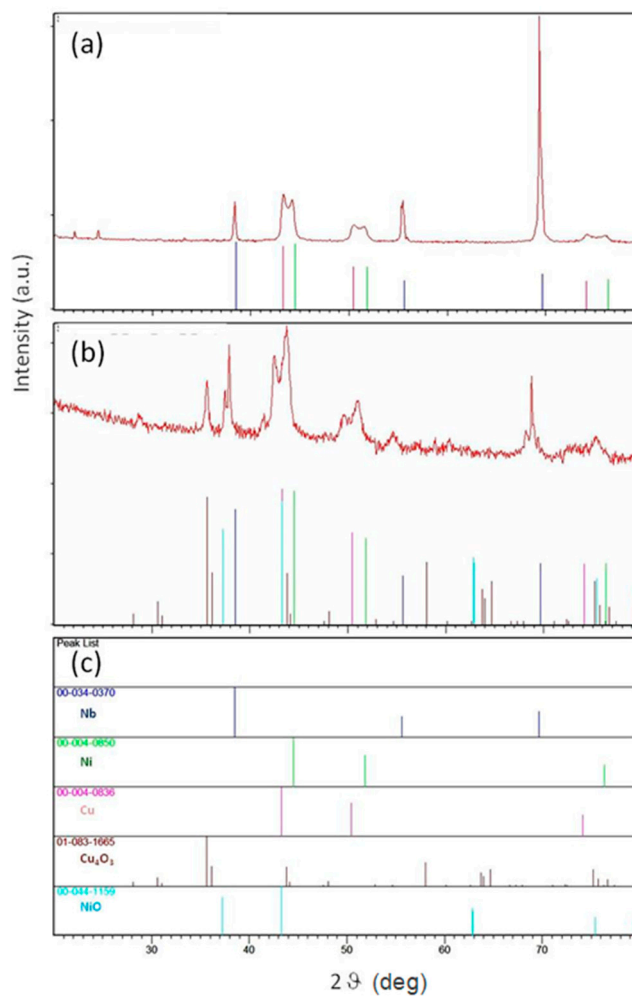
Figure 3. XRD pattern of the films as-deposited (**a**) and of the sample S$_{1-5}$ after the corrosion (**b**) and relevant PDF cards for reference structures.
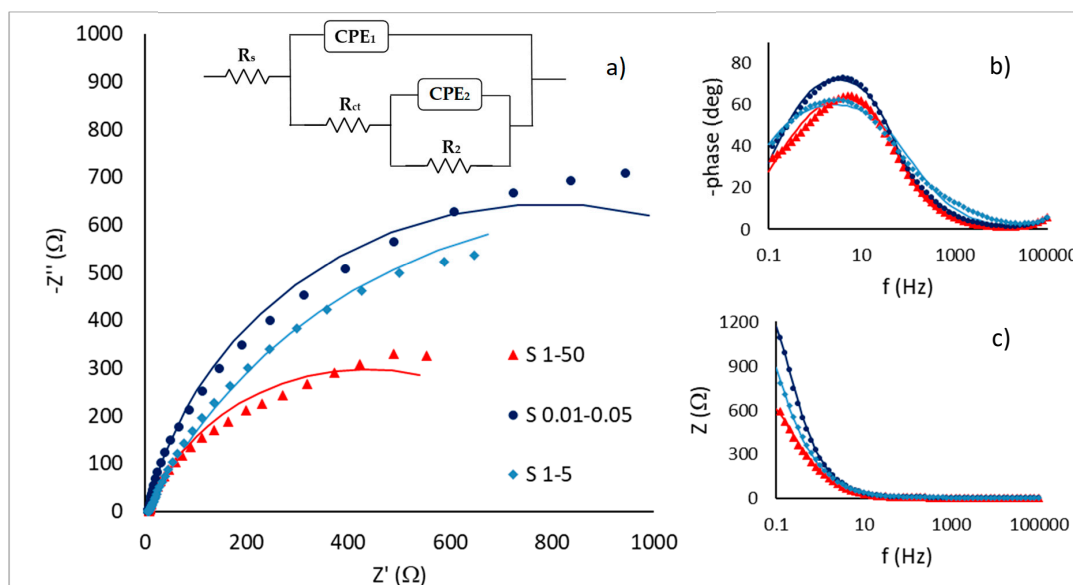
Figure 4. Nyquist diagram (**a**), Bode phase (**b**) and Bode modulus (**c**) recorded in KOH 1 M at open circuit potential. Inset: equivalent circuit used to model the EIS spectra.

To model the experimental data, an electrochemical equivalent circuit, which involves two time constants, was used (inset of Figure 4): the model is a slightly modified version of that originally proposed by Armstrong and Henderson [43], in which the capacitances were replaced by the constant phase elements (CPE) [44–46] which represent a deviation from the purely capacitive behaviour, related to surface in-homogeneity, or to variations of properties in the direction that is normal to the electrode surface. Such variability may be attributed, for example, to changes in the conductivity of oxide layers, or to porosity and surface roughness [47].
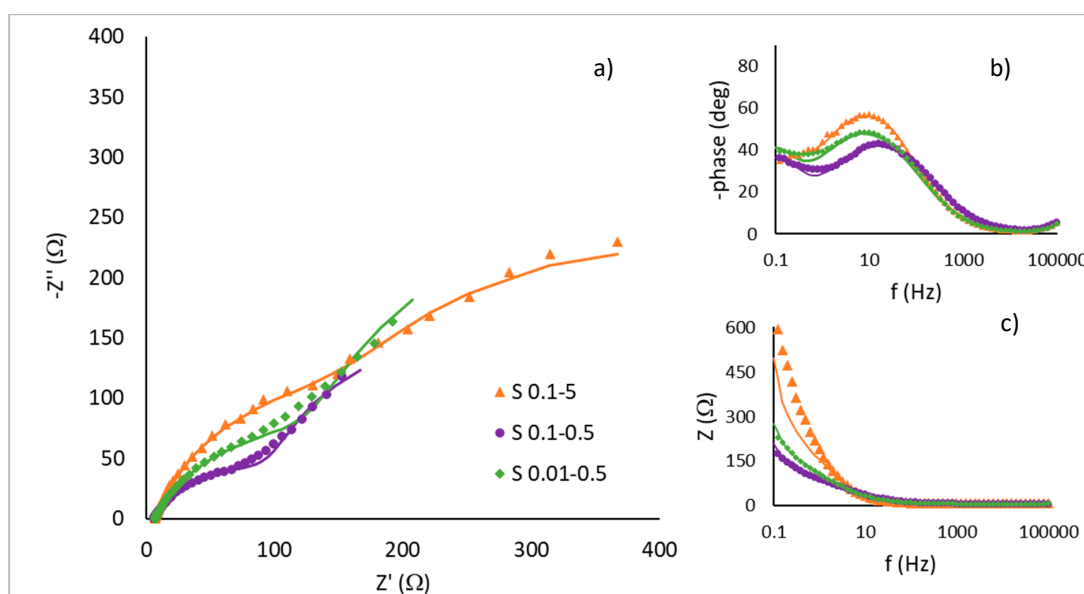
Figure 5. Nyquist diagram (**a**), Bode phase (**b**) and Bode modulus (**c**) recorded in KOH 1 M at open circuit potential.

The impedance Z_{CPE} is described by the following equation:

$$Z_{CPE} = \frac{1}{Q(j\omega)^n} \qquad (1)$$

where Q is a capacitance parameter and n is a parameter characterizing the rotation of the complex plane impedance plot [47].

This two time constants model was widely used to describe the response of Ni-based porous electrodes during HER; when the semicircle at HF is potential-independent, it can be related to the electrode surface porosity response, while the potential-dependent LF semicircle can be related to the charge transfer resistance process [44,48,49]. On the other hand, when both semicircles change with overpotential, the LF time constant is associated to the hydrogen adsorption on the electrode surface, while the HF time constant is related to the charge transfer resistance [48,50].

In the present work, the same electrical circuit was used to model the response of the porous electrodes at OCP and the different time constants were correlated to the different pore size distribution. Analogous approach was adopted with hierarchical structures by Abouelamaiem et al. [51]: the smaller the pores, the higher the constant time values.

As can be seen from Figures 4 and 5, in the present case, the proposed model was able to interpret the Nyquist and Bode plots of the selected samples. The fitting parameters are presented in Table 2, along with the values of chi-squared (χ^2), which were always in the order of 10^{-4}.

Table 2. Electrical circuital parameters obtained from the fit of EIS spectra at open circuit potential for the synthesized samples, recorded in KOH 1 M.

Samples	S_{1-5}	$S_{0.1-0.5}$	$S_{0.01-0.05}$	S_{1-50}	$S_{0.1-5}$	$S_{0.01-0.5}$
χ^2	2.06×10^{-4}	8.33×10^{-4}	7.69×10^{-4}	9.51×10^{-4}	5.84×10^{-4}	9.82×10^{-4}
R_s/Ω cm^2	3.16	3.16	3.44	3.70	3.28	3.38
R_{ct}/Ω cm^2	829	65.90	784.5	433.4	140.65	103.60
Q_1/mS s^n cm^{-2}	0.52	3.18	0.242	0.76	1.99	3.24
n_1	0.86	0.68	1.00	1.00	0.80	0.72
R_2/Ω cm^2	6.055	141.4	4.71	3.4	157.7	239.8
Q_2/mS s^n cm^{-2}	1.60	16.66	1.17	2.08	6.82	12.14
n_2	0.71	1.00	0.85	0.73	0.99	1.00
$C_{dl}/\mu F$ cm^{-2}	454	1522	242	760	1439	2118
$C_2/\mu F$ cm^{-2}	250	16660	460	335	6821	12140
τ_1 (s)	0.38	0.10	0.19	0.33	0.20	0.22
τ_2 (s)	0.0015	2.36	0.0022	0.0011	1.08	2.91
R_f	22.7	76.1	12.1	38.0	71.9	105.9
A_r (cm^2)	11	38	6	19	36	53

Table 2 reports also the values of capacitance (C) calculated as proposed by Brug et al. [52] for non-Faradaic system:

$$C_i = \frac{(Q_i R_i)^{1/n_i}}{R_i} \tag{2}$$

and the time constant (τ)

$$\tau_i = C_i R_i \tag{3}$$

Depending on the samples, different time constant values are calculated from the relevant circuital parameters, that can give information on the processes occurring at the electrode surface.

So, for example, the values of τ_1 between 0.10 and 0.38 s, are in the order of magnitude typically related to the charge transfer between electrode/electrolyte interface. Time constants in the order of half second were reported by Cardona et al [48,53], for porous Ni and Ni-Cu electrodes, and were attributed to the charge transfer kinetics. On the other hand, as suggested by other references [46,50,53], the τ_2 values 10-fold higher, calculated for samples $S_{0.1-0.5}$, $S_{0.1-5}$, $S_{0.01-0.5}$, could be instead associated to the diffusion inside the smaller, less accessible pores. Finally, a very fast charge transfer inside the bulk material should be the reason of the very low values of τ_2 (in the order of ms) calculated for samples S_{1-5}, $S_{0.01-0.05}$, S_{1-50}.

This different behavior can be explained considering the different morphology of the samples: when a tubular structure with little variations of the pore diameter is obtained, as in the case of sample S_{1-5}, the response of the impedance is dominated by accessible surface inside the pores. Conversely, when a multidimensional pores structure, such as a cauliflower-like surface is obtained (see for example sample $S_{0.01-0.5}$), the slow diffusive process in the smaller pores may become important, given that it is revealed when low frequency region is explored.

The values of C_{dl} were used, in turn, to compare the real surface area of the samples accessible to the electrolyte: the surface roughness factor R_f, was determined relating the C_{dl} of the samples with that of a smooth Ni electrode equal to 20 $\mu F/cm^2$ [46] an in turn, the values of real active surface area (A_r) were calculated (see Table 2).

The results reported in Table 2 highlight that the group of samples prepared using a lower ϕ presents higher values of C_{dl} and of roughness factor (R_f). Moreover, at the same ϕ values, an increase in the porosity is recorded with the decrease of the corrosion and relaxation time. This is not verified in the case of the sample $S_{0.01-0.05}$, where very low pore density was obtained. Moreover, R_f values of 8 and 13 were obtained by EIS at commercial nickel plate and at Ni-Cu co-deposit, respectively.

In the last part of the work attention was paid on the evaluation of the catalytic activity of the samples toward HER. As is well known, especially when heterogeneous reactions are involved, the

achievement of high specific area is of a great concern. However, also the morphology, and then the exploitability of the surface, may affect the material performances, particularly when the reactions involve the production of gas, as in the case of HER. Moreover, a synergistic effect on the catalytic activity was often attributed to the presence of copper, either in alloy, or co-deposited with nickel.

In order to study these effects, two samples were selected, which were characterized by different roughness factor, morphology and residual copper content: in particular, S_{1-5} was selected among those with $\phi = 0.2$, and $S_{0.01-0.5}$ among those with $\phi = 0.02$ (see Table 1). Their electrocatalytic performance and their photoactivity were investigated, and their behavior compared with those of commercial nickel plate and Ni-Cu co-deposit.

Figure 6 reports the results of linear sweep polarization curves, performed in 1 M KOH solution: the cathodic current densities are reported as a function of the overpotential (η) together with the corresponding Tafel linearization, as inset.
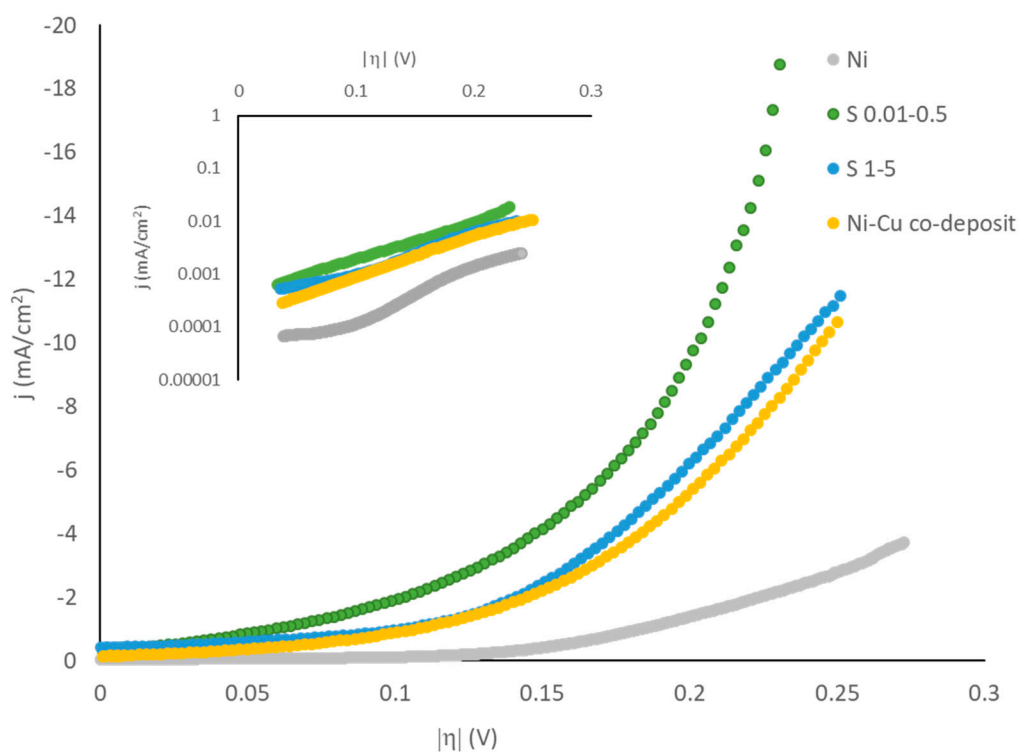
Figure 6. Linear sweep voltammetries in 1 M KOH solution; inset: magnification of the linear Tafel polarization curves.

If compared with commercial nickel plate, the samples S_{1-5} and $S_{0.01-0.5}$ present higher catalytic activity, the highest being obtained for sample $S_{0.01-0.5}$. This enhancement in the catalytic activity can be connected to the increased specific surface area. Moreover, the trend of the linear sweep polarization of the Cu-Ni co-deposit indicates the positive effect of the presence of copper.

The kinetic parameters of the related processes were determined by considering both the geometric and the real surface area of the electrodes. The polarization curves are represented by Tafel equation [54]:

$$\eta = a + b \, log \, j \tag{4}$$

where η is the overpotential, b is the Tafel slope, j is the current density and a is the intercept of the curve related to the exchange current density j_0 through equation:

$$a = \frac{2.3 \, RT}{\beta nF} log \, j_0 \tag{5}$$

where *n* represents the number of electrons exchanged, *F* is the Faraday constant, *β* is the symmetry factor and *R* is the gas constant.

Values of exchange current density j_0, and Tafel slope *b*, estimated from the linear polarization curves using Equations (4) and (5), are listed in Table 3.

As can be observed, the values of Tafel slope (*b*) obtained for the synthesized samples range from 126 to 140 mV/dec, indicating that HER proceeds via the Volmer-Heyrosky mechanism [44,55]; similar values were reported in the literature for porous Ni-based samples also in presence of copper [46,48]. Both samples $S_{1–5}$ and $S_{0.01–0.5}$ present exchange current density values considerably higher with respect to the commercial nickel, indicating a considerable improvement of the apparent electrocatalytic properties of the fabricated electrodes.

Table 3. Kinetic parameters for HER obtained from the polarization curves recorded in 1 M KOH.

| Sample	Rf	b (mV/dec)	j_0 (mA/cm^2)	j_{0r} (μA/cm^2)
Ni	8	130	0.02	4.2
Cu-Ni co-deposit	13	124	0.13	12
$S_{1–5}$	23	158	0.29	8.6
$S_{0.01–0.5}$	106	138	0.35	4.6

The value measured for the Ni-Cu co-deposit is instead indicative of the effect of the presence of copper in the deposit. Normalizing the exchange current densities for the active surface area of the electrodes, the real exchange current density j_{0r} was calculated.

The higher j_{0r} value for the sample $S_{1–5}$ with respect to that for $S_{0.01–0.5}$, suggests that the inner porous surface of this sample is not totally exploitable during HER, due to the gas bubbles shielding. This behavior can be explained by considering the more open structure of sample $S_{1–5}$ with respect to $S_{0.01–0.5}$, thus confirming the strong effect of the pores (size, shape and distribution) on the resulting electrocatalytic performance. Comparing the j_{0r} values for sample $S_{1–5}$ with that of commercial nickel, the effect of the composition of the sample can be observed: in fact, the enhancement in the performance is not only related to the increased surface area, but also to the copper amount which affects the overall electroactivity of the electrodes. This effect can be confirmed at Ni-Cu co-deposit, where the enhancement of j_{0r}, compared to a commercial nickel electrode, can be connected essentially to the presence of a rough dual Ni-Cu system.

In order to investigate possible applications of the developed samples as photocathodes, they were submitted to thermal annealing at 500 °C in order to allow the formation of NiO.

Figure 7 shows, as an example, the cathodic photocurrent response measured at sample $S_{0.01–0.5}$: as can be seen, under irradiation a remarkable increase in photocurrent is observed.

In order to compare the photocurrent of samples $S_{1–5}$, $S_{0.01–0.5}$ and commercial nickel, in Figure 8 the values of photocurrent are reported for three values of applied potential; as can be seen, applied potential being the same, samples $S_{1–5}$ and $S_{0.01–0.5}$ present higher values of photocurrent with respect to the commercial nickel. These values are comparable with those reported in the literature and measured in similar conditions: for NiO photocathodes fabricated by alkaline etching, anodizing nickel foil in an organic-based electrolyte, about 400 μA/cm^2 was measured irradiating the samples with 300 W arc xenon lamp [15]. The values in the order of magnitude of the tens were indicated in a recent review, where sensitized NiO photocathodes for water splitting cells were used: the authors state that photocurrent values varied consistently with the specific surface area of the electrode, suggesting that NiO electrodes made under different conditions should possess comparable photoelectrochemical performance [56].
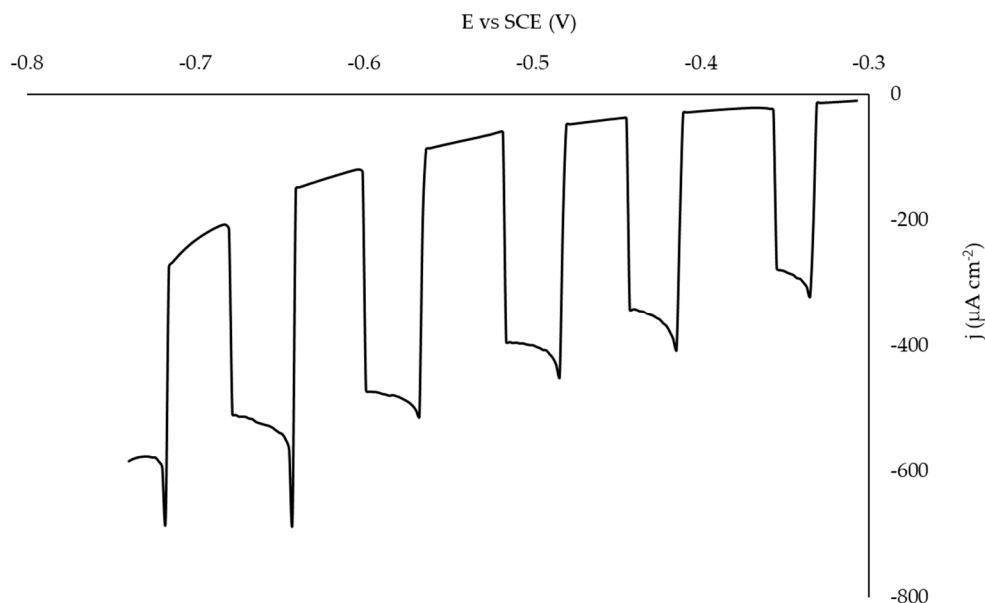
Figure 7. LSV of sample $S_{0.01-0.5}$ in 0.1 M KNO_3. The potential was ramped (5 mV s^{-1}) from the OCP to -0.8 V. Data were recorded under dark and irradiation condition (AM0 filter).
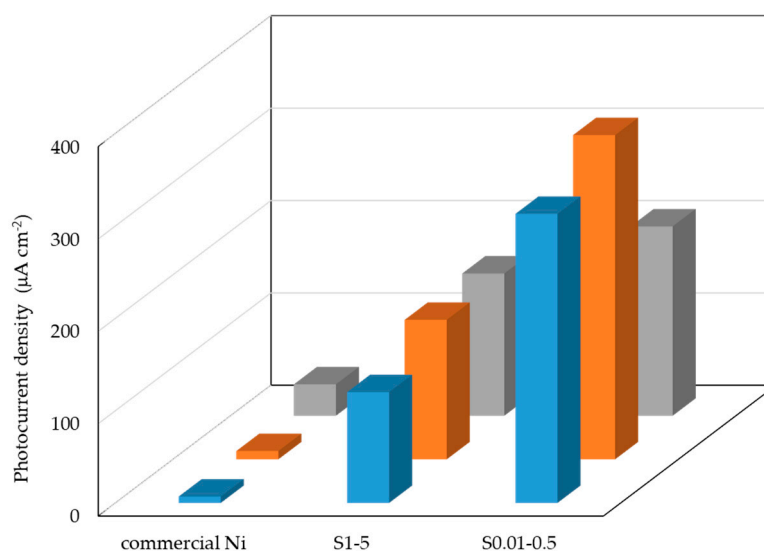
Figure 8. Cathodic photocurrent density recorded in KNO_3 0.1 M solution for different samples, at different applied potential: -0.4 V (blue bars), -0.6 V (orange bars) and -0.8 V (grey bars).

If data at different applied potential are considered, a different behavior of S_{1-5} and $S_{0.01-0.5}$ samples can be observed: as the cathodic potential is increased, while a regular increase in performance is measured at sample S_{1-5}, sample $S_{0.01-0.5}$ shows lower value of photocurrent when the most cathodic potentials is applied. This trend may be explained considering that at the highest cathodic potential, gas can be generated which may limit the exploitability of the whole pore structure, especially when small pores are involved in the structure, as at sample $S_{0.01-0.5}$. Of note is that if the photocurrent values are normalized by the real surface area (A_r) of the samples, the highest performance is measured at sample S_{1-5}, at all the potentials; moreover, at the highest cathodic potential, the performance of $S_{0.01-0.5}$ sample decreases, and it becomes even worst than the commercial Ni sample.

3. Materials and Methods

Boric acid (H_3BO_3) and potassium hydroxide (KOH) were purchased from Sigma-Aldrich (Sigma-Aldrich Chemie, GmbH, Schnelldorf; Germany). Sodium sulfate anhydrous (Na_2SO_4), nickel sulfate hexahydrate ($NiSO_4*6H_2O$), copper sulfate pentahydrate ($CuSO_4*5H_2O$) and potassium nitrate (KNO_3) were supplied by Carlo Erba (Carlo Erba Reagents, Cornaredo, Milano, Italy). All electrochemical experiments were performed at room temperature using an AUTOLAB PGSTAT302N (Metrohm, Herisau, Switzerland) potentiostat/galvanostat equipped with a frequency response analyzer controlled with the NOVA software. Two cylindrical hand-made three-electrode cells realized by Teflon were used, in which the working electrode was at the bottom of the cell and the electrical contact consisted of an aluminium disc. A platinized titanium grid, placed in front of the anode at 1 cm distance, and a saturated calomel electrode (SCE) constituted the counter and reference electrodes, respectively. The preparation of the Ni-Cu co-deposits was performed using niobium foils (thickness 0.25 mm, 99.8%, Sigma-Aldrich Chemie, GmbH, Schnelldorf; Germany) as working electrode, cut as discs. Prior to deposition, niobium was mechanically polished with diamond paste (sizes: 3, 1, 0.5 μm) and colloidal silica gel (particles size: 0.05 μm), then submitted to sonication in acetone for 15 minutes and rinsed with distilled water. The cell used for the electrodeposition experiment contained 40 ml of solution (inner diameter = 5 cm, height 4 cm); the exposed geometrical area was 13.5 cm^2. The electrodeposition was performed using solution containing 0.5 M $NiSO_4$, 0.005 M $CuSO_4$ and 0.5 M H_3BO_4 (pH = 4); linear sweep voltammetry was firstly performed in the electrodeposition solution at 5 mV s^{-1}, starting from the OCP up to −0.8 V, after that a constant potential of −0.8 V for a total time of 130 minutes was applied while the solution was stirred. The charge amount recorded during the electrodeposition experiments was about 6 C/cm^2. Considering unit faradaic yield and average atomic weight of 60 g/mol, the amount of deposited metals was roughly estimated equal to 1.8 mg/cm^2, by Faraday's Law.

In order to study the effect of the selective corrosion, starting from the same co-deposit, after the deposition the discs were cut in six slices and subjected to anodic dissolution under different corrosion conditions. The cell used for corrosion experiment contained 10 ml of solution (inner diameter = 1.5 cm, height 3 cm): the exposed geometrical area was 0.5 cm^2.

The runs were performed in aqueous solution, containing 0.5 M H_3BO_4 and 0.5 M Na_2SO_4, under stirring conditions, using pulsed voltage modulated between V_{corr} (E = 0.5 V) and V_{relax} (E = OCP) for time durations of t_{corr} and t_{relax}, respectively. Values of the ratio between t_{corr} and t_{relax} (called ϕ in the rest of the text) equal to 0.2 and 0.02 were adopted. A total time of 30 minutes were required (typically the dissolution current drops to zero within this period). Prepared samples were denoted as $S_{tcorr-trelax}$ where t_{corr} and t_{relax} are the corrosion and relaxation times (in seconds), respectively. After oxidation, the electrodes were rinsed in deionized water and dried in a nitrogen stream. The charges amount, recorded during the corrosion test, ranged from 1.2 to 1.6 C/cm^2. Also in this case, applying Faraday's Law, the amount of copper removed was evaluated from 0.4 to 0.55 mg/cm^2.

A scanning electron microscope (SEM) equipped with EDX detector (Zeiss, Oberkochen, Germany) was used to characterize the morphology and the chemical composition of the nanoporous nickel electrodes. Auger electron Spectroscopy (AES) was also used to investigate the distribution of the copper and nickel.

X-ray diffraction (XRD) patterns were recorded in the range of 20–80 (2θ) on a Panalytical Empyrean diffractometer equipped with a Cu Kα radiation and an X'Celerator linear detector. XRD patterns were collected at a grazing incidence of 2 on the films mounted on a flat sample stage. Data were processed by Empyrean X'pert High Score software and phase identification was performed by comparison with the Powder Diffraction Files (PDF-2 JCPDS International Centre for Diffraction Data, Swarthmore, PA, USA) database.

Linear sweep voltammetry (LSV) were performed to study the behavior of the electrodes in the potential range from E = OCP to E = −1.0 V in cathodic direction at a sweep rate of 5 mV/s. The characterization of the electrode/electrolyte interface was also carried out through electrochemical

impedance spectroscopy (EIS). The measurements were performed in a frequency range from 100 kHz to 0.1 Hz with excitation amplitude of 10 mV. The impedance spectra were then fitted to an equivalent electrical circuit by using the ZSimpWin 2.0 software (EChem software).

A subsequent annealing treatment was performed in order to convert $Ni(OH)_2$ and NiOOH groups in NiO, which is the semiconductive form of nickel. Thermal treatment was carried out in air atmosphere for 30 min at 500 °C, after ramping 5 °C min^{-1}.

Photoelectrochemical measurements were carried out in a hand-made photoelectrochemical cell (PEC), equipped with a quartz window. The investigated samples were adopted as working electrodes while a platinum wire constituted the counter electrode and a SCE the reference. 0.1 M KNO_3 aqueous solution was used as the supporting electrolyte. The PEC-cell was irradiated with a 300 W Xe lamp (LOT-Quantum Design Europe) equipped with AM 0 optical filter. The incident power density of the light was measured by LP 471 UVU or LP 471 PAR quantum radiometric probes: the recorded value was 138–140 W/m^2. Photocurrent density was calculated with respect the nominal surface area of the samples as the difference between the current recorded under illumination and dark conditions.

4. Conclusions

In this work, a dealloying method was used to obtain porous nickel electrodes as possible alternative cathodic materials in HER. A suitable combination of corrosion and relaxation times in the pulsed potential steps made it possible to obtain different morphologies and pore size distributions. Depending on the samples, roughness factors ranging from 22 and 106 were obtained, but the increased surface area was not always exploitable. In fact, the Tafel analysis revealed that the exchange current density calculated with respect to the real surface area, was higher in sample S_{1-5} rather than sample $S_{0.01-0.5}$, even if a higher surface area was measured at this last sample. The higher j_{0r} value suggests that the inner porous surface area of sample $S_{0.01-0.5}$ is not totally exploitable during HER, due to gas bubbles shielding. This behavior can be explained by considering the more open structure of sample S_{1-5} with respect to $S_{0.01-0.5}$, thus confirming the strong effect of the pores (size, shape and distribution) on the resulting electrocatalytic performance. The presence of thin oxide layer of NiO, as well as of residual copper were indicated as responsible for the photocatalytic activity of the samples. Once again, the different pore size and distribution become crucial in determining the final performance of the samples: thus, for example, at the highest cathodic potential gas can be generated which may limit the exploitability of the whole pore structure, especially when small pores are involved in the structure, as at sample $S_{0.01-0.5}$.

Conflicts of Interest: The authors declare no conflict of interest.

References

1. Zhao, G.; Rui, K.; Dou, S.X.; Sun, W. Heterostructures for Electrochemical Hydrogen Evolution Reaction: A Review. *Adv. Funct. Mater.* **2018**, *28*, 1803291. [CrossRef]
2. Murthy, A.P.; Madhavan, J.; Murugan, K. Recent advances in hydrogen evolution reaction catalysts on carbon/carbon-based supports in acid media. *J. Power Sources* **2018**, *398*, 9–26. [CrossRef]
3. Eftekhari, A. Electrocatalysts for hydrogen evolution reaction. *Int. J. Hydrog. Energy* **2017**, *42*, 11053–11077. [CrossRef]
4. Kibsgaard, J.; Jaramillo, T.F.; Besenbacher, F. Building an appropriate active-site motif into a hydrogen-evolution catalyst with thiomolybdate $[Mo_3S_{13}]^{2-}$ clusters. *Nat. Chem.* **2014**, *6*, 248–253. [CrossRef] [PubMed]

5. Chang, Y.H.; Lin, C.T.; Chen, T.Y.; Hsu, C.L.; Lee, Y.H.; Zhang, W.; Wei, K.H.; Li, L.J. Highly efficient electrocatalytic hydrogen production by MoSx grown on graphene-protected 3D Ni foams. *Adv. Mater.* **2013**, *25*, 756–760. [CrossRef]

6. Youn, D.H.; Han, S.; Kim, J.Y.; Kim, J.Y.; Park, H.; Choi, S.H.; Lee, J.S. Highly active and stable hydrogen evolution electrocatalysts based on molybdenum compounds on carbon nanotube-graphene hybrid support. *ACS Nano* **2014**, *8*, 5164–5173. [CrossRef] [PubMed]

7. Chen, W.F.; Muckerman, J.T.; Fujita, E. Recent developments in transition metal carbides and nitrides as hydrogen evolution electrocatalysts. *Chem. Commun.* **2013**, *49*, 8896–8909. [CrossRef]

8. Faber, M.S.; Jin, S. Earth-abundant inorganic electrocatalysts and their nanostructures for energy conversion applications. *Energy Environ. Sci.* **2014**, *7*, 3519–3542. [CrossRef]

9. Yu, X.Y.; Feng, Y.; Guan, B.; Lou, X.W.; Paik, U. Carbon coated porous nickel phosphides nanoplates for highly efficient oxygen evolution reaction. *Energy Environ. Sci.* **2016**, *9*, 1246–1250. [CrossRef]

10. Zhao, Z.; Wu, H.; He, H.; Xu, X.; Jin, Y. A high-performance binary Ni-Co hydroxide-based water oxidation electrode with three-dimensional coaxial nanotube array structure. *Adv. Funct. Mater.* **2014**, *24*, 4698–4705. [CrossRef]

11. Zhang, G.; Yuan, J.; Liu, Y.; Lu, W.; Fu, N.; Lia, W.; Huang, H. Boosting the oxygen evolution reaction in non-precious catalysts by structural and electronic engineering. *J. Mater. Chem. A* **2018**, *6*, 10253–10263. [CrossRef]

12. Wei, J.; Zhou, M.; Long, A.; Xue, Y.; Liao, H.; Wei, C.; Xu, Z.J. Heterostructured Electrocatalysts for Hydrogen Evolution Reaction Under Alkaline Conditions. *Nano-Micro Lett.* **2018**, *10*, 75. [CrossRef] [PubMed]

13. Liu, X.; Wang, X.; Yuang, X.; Dong, W.; Huang, F. Rational composition and structural design of in situ grown nickel-based electrocatalysts for efficient water electrolysis. *J. Mater. Chem. A* **2016**, *4*, 167–172. [CrossRef]

14. Macdonald, T.J.; Xu, J.; Elmas, S.; Mange, Y.J.; Skinner, W.M.; Xu, H.; Nann, T. NiO Nanofibers as a Candidate for a Nanophotocathode. *Nanomaterials* **2014**, *4*, 256–266. [CrossRef] [PubMed]

15. Hu, C.; Chu, K.; Zhao, Y.; Teoh, E.Y. Efficient Photoelectrochemical Water Splitting over Anodized p Type NiO Porous Films. *ACS Appl. Mater. Interfaces* **2014**, *6*, 18558–18568. [CrossRef]

16. Li, L.; Gibson, E.A.; Qin, P.; Boschloo, G.; Gorlov, M.; Hagfeldt, A.; Sun, L. Double-Layered NiO Photocathodes for p-Type DSSCs with Record IPCE. *Adv. Mater.* **2010**, *22*, 1759–1762. [CrossRef] [PubMed]

17. Wu, L.; Guo, X.; Xu, Y.; Xiao, Y.; Qian, J.; Xu, Y.; Guan, Z.; He, Y.; Zeng, Y. Electrocatalytic activity of porous Ni–Fe–Mo–C–LaNi$_5$ sintered electrodes for hydrogen evolution reaction in alkaline solution. *RSC Adv.* **2017**, *7*, 32264–32274. [CrossRef]

18. Arce, E.M.; Lopez, V.M.; Martinez, L.; Dorantes, H.J.; Saucedo, M.L.; Hernandez, F. Electrocatalytic properties of mechanically alloyed Co-20 wt % Ni-10 wt % Mo and Co-70 wt % Ni-10 wt % Mo alloy powders. *J. Mater. Sci.* **2003**, *38*, 275–278. [CrossRef]

19. Kedzierzawski, P.; Oleszak, D.; Janik-Czachor, M. Hydrogen evolution on hot and cold consolidated Ni-Mo alloys produced by mechanical alloying. *Mater. Sci. Eng. A* **2001**, *300*, 105–112. [CrossRef]

20. Ngamlerdpokin, K.; Tantavichet, N. Electrodeposition of nickel–copper alloys to use as a cathode for hydrogen evolution in an alkaline media. *Int. J. Hydrog. Energy* **2014**, *39*, 2505–2515. [CrossRef]

21. Solmaz, R.; Döner, A.; Kardaş, G. Electrochemical deposition and characterization of NiCu coatings as cathode materials for hydrogen evolution reaction. *Electrochem. Commun.* **2008**, *10*, 1909–1911. [CrossRef]

22. Friend, W.Z. *Corrosion of Nickel and Nickel Alloys*; Wiley-Interscience: Manhattan, NY, USA, 1980.

23. Solmaz, R.; Döner, A.; Kardaş, G. The stability of hydrogen evolution activity and corrosion behavior of NiCu coatings with long-term electrolysis in alkaline solution. *Int. J. Hydrog. Energy* **2009**, *34*, 2089–2094. [CrossRef]

24. Bae, J.H.; Han, J.-H.; Chung, T.D. Electrochemistry at nanoporous interfaces: New opportunity for electrocatalysis. *Phys. Chem. Chem. Phys.* **2012**, *14*, 448–463. [CrossRef] [PubMed]

25. Dominguez Crespo, M.A.; Plata Torres, M.; Torres Huerta, A.M.; Ortiz Rodriguez, I.A.; Ramirez Rodriguez, C.; Arce Estrada, E.M. Influence of Fe contamination and temperature on mechanically alloyed Co-Ni-Mo electrodes for hydrogen evolution reaction in alkaline water. *Mater. Charact.* **2006**, *56*, 138–146. [CrossRef]

26. Aymard, L.; Dumont, B.; Viau, G. Production of Co-Ni alloys by mechanical-alloying. *J. Alloys Compd.* **1996**, *242*, 108–113. [CrossRef]

27. Zhang, J.; Li, C.M. Nanoporous metals: fabrication strategies and advanced electrochemical applications in catalysis, sensing and energy systems. *Chem. Soc. Rev.* **2012**, *41*, 7016–7031. [CrossRef]

28. Martínez, W.; Fernández, A.; Cano-Castillo, U. Synthesis of nickel-based skeletal catalyst for an alkaline electrolyzer. *Int. J. Hydrog. Energy* **2010**, *35*, 8457–8462. [CrossRef]

29. Olurin, O.B.; Wilkinson, D.S.; Weatherly, G.C.; Paserin, V.; Shu, J. Strength and ductility of as-plated and sintered CVD nickel foams. *Compos. Sci. Technol.* **2003**, *63*, 2317–2329. [CrossRef]

30. Paserin, V.; Marcuson, S.; Shu, J.; Wilkinson, D.S. CVD Technique for Inco Nickel Foam Production. *Adv. Eng. Mater.* **2004**, *6*, 454–459. [CrossRef]

31. Marozzi, C.; Chialvo, A. Development of electrode morphologies of interest in electrocatalysis. Part 1: Electrodeposited porous nickel electrodes. *Electrochim. Acta* **2000**, *45*, 2111–2120. [CrossRef]

32. Li, Y.; Xiao, X.; Zhao, R.; Yu, K.; Hou, C.; Liang, J. Study of the fabrication and characterization of porous ni using polystyrene sphere template. *Synth. React. Inorg. Met.-Org. Nano-Met. Chem.* **2016**, *46*, 286–290. [CrossRef]

33. Böhme, O.; Leidich, F.U.; Salge, H.J.; Wendt, H. Development of materials and production technologies for molten carbonate fuel cells. *Int. J. Hydrog. Energy* **1994**, *19*, 349–355. [CrossRef]

34. Rahman, A.; Zhu, X.; Wen, C. Fabrication of Nanoporous Ni by chemical dealloying Al from Ni-Al alloys for lithium-ion batteries. *Int. J. Electrochem. Sci.* **2015**, *10*, 3767–3783.

35. Sun, L.; Chien, C.L.; Searson, P.C. Fabrication of Nanoporous Nickel by Electrochemical Dealloying. *Chem. Mater.* **2004**, *16*, 3125–3129. [CrossRef]

36. Chang, J.K.; Hsu, S.H.; Sun, I.W.; Tsai, W.T. Formation of Nanoporous Nickel by Selective Anodic Etching of the Nobler Copper Component from Electrodeposited Nickel–Copper Alloys. *J. Phys. Chem. C* **2008**, *112*, 1371–1376. [CrossRef]

37. Jeong, M.G.; Zhuo, K.; Cherevko, S.; Chung, C.H. Formation of nanoporous nickel oxides for supercapacitors prepared by electrodeposition with hydrogen evolution reaction and electrochemical dealloying. *Korean J. Chem. Eng.* **2012**, *29*, 1802–1805. [CrossRef]

38. Zhang, J.; Zhan, Y.; Bian, H.; Li, Z.; Tsang, C.K.; Lee, C.; Cheng, H.; Shu, S.; Li, Y.Y.; Lu, J. Electrochemical dealloying using pulsed voltage waveforms and its application for supercapacitor electrodes. *J. Power Sources* **2014**, *257*, 374–379. [CrossRef]

39. Erlebacher, J.; Aziz, M.J.; Karma, A.; Dimitrov, N.; Sieradzki, K. Evolution of nanoporosity in dealloying. *Nature* **2001**, *410*, 450–453. [CrossRef] [PubMed]

40. Losiewicz, B.; Budniok, A.; Rowinski, E.; Lagiewka, E.; Lasia, A. The structure, morphology and electrochemical impedance study of the hydrogen evolution reaction on the modified nickel electrodes. *Int. J. Hydrog. Energy* **2004**, *29*, 145–157. [CrossRef]

41. Panek, J.; Serek, A.; Budniok, A.; Rowinski, E.; Lagiewka, E. Ni + Ti composite layers as cathode materials for electrolytic hydrogen evolution. *Int. J. Hydrog. Energy* **2003**, *28*, 169–175. [CrossRef]

42. Hiltz, C.; Lasia, A. Experimental study and modeling of impedance of the her on porous Ni electrodes. *J. Electroanal. Chem.* **2001**, *500*, 213–222. [CrossRef]

43. Armstrong, R.D.; Henderson, M. Impedance plane display of a reaction with an adsorbed intermediate. *J. Electroanal. Chem.* **1972**, *39*, 81–90. [CrossRef]

44. Lasia, A.; Rami, A. Kinetics of hydrogen evolution on Nickel electrodes. *J. Electroanal. Chem.* **1990**, *294*, 123–141. [CrossRef]

45. Birry, L.; Lasia, A. Studies of the hydrogen evolution reaction on Raney nickel molybdenum electrodes. *J. Appl. Electrochem.* **2004**, *34*, 735–749. [CrossRef]

46. Herraiz-Cardona, I.; Ortega, E.; Vazquez-Gomez, L.; Perez-Herranz, V. Double-template fabrication of three-dimensional porous nickel electrodes for hydrogen evolution reaction. *Int. J. Hydrog. Energy* **2012**, *37*, 2147–2156. [CrossRef]

47. Orazem, M.E.; Tribollet, B. *Electrochemcial Impedance Spectroscopy*; John Wiley & Sons, Inc.: Hoboken, NJ, USA, 2008.

48. Herraiz-Cardona, I.; Ortega, E.; Pérez-Herranz, V. Impedance study of hydrogen evolution on Ni/Zn and Ni–Co/Zn stainless steel based electrodeposits. *Electrochim. Acta* **2011**, *56*, 1308–1315. [CrossRef]

49. Borresen, B.; Hagen, G.; Tunold, R. Hydrogen evolution on $Ru_xTi_{1-x}O_2$ in 0.5 M H_2SO_4. *Electrochim. Acta* **2002**, *47*, 1819–1827. [CrossRef]

50. Castro, E.B.; De Giz, M.J.; Gonzalez, E.R.; Vilche, J.R. An electrochemical impedance study on the kinetics and mechanism of the hydrogen evolution reaction on nickel molybdenite electrodes. *Electrochim. Acta* **1997**, *42*, 951–959. [CrossRef]

51. Abouelamaiem, D.I.; He, G.; Neville, T.P.; Patel, D.; Ji, S.; Wang, R.; Parkin, I.P.; Jorge, A.B.; Titirici, M.M.; Shearing, P.R.; et al. Correlating electrochemical impedance with hierarchical structure for porous carbon-based supercapacitors using a truncated transmission line model. *Electrochim. Acta* **2018**, *284*, 597–608. [CrossRef]

52. Brug, G.J.; Van den Eeden, A.L.G.; Sluyters-Rehbach, M.; Sluyters, J.H. The Analysis of Electrode Impedances Complicated by the Presence of a Constant Phase Element. *J. Electroanal. Chem.* **1984**, *176*, 275–295. [CrossRef]

53. Valero-Vidal, C.; Herraiz-Cardona, I.; Pérez-Herranz, V.; Igual-Munoz, A. Stability of 3D-porous Ni/Cu cathodes under real alkaline electrolyzer operating conditions and its effect on catalytic activity. *Appl. Catal. B Environm.* **2016**, *198*, 142–153. [CrossRef]

54. Pletcher, D.; Greff, R.; Peat, R.; Peter, L.M.; Robinson, J. *Instrumental Methods in Electrochemistry*; Woodhead Publishing Limited: Philadelphia, PA, USA, 2010.

55. Delgado, D.; Minakshi, M.; Kim, D.J.; Kyeong, C.W. Influence of the Oxide Content in the Catalytic Power of Raney Nickel in Hydrogen Generation. *Anal. Lett.* **2017**, *50*, 2386–2401. [CrossRef]

56. Xu, P.; McCool, N.S.; Mallouk, T.E. Water splitting dye-sensitized solar cells. *Nano Today* **2017**, *14*, 42–58. [CrossRef]